Robotica (2010) volume 28, pp. 705–718. © Cambridge University Press 2009
doi:10.1017/S0263574709990397

Autonomous rendezvous and robotic capturing of non-cooperative target in space

Wenfu Xu†,‡,*, Bin Liang†, Cheng Li† and Yangsheng Xu§

†*The Institute of Space Intelligent System, Harbin Institute of Technology, Harbin, P.R. China*
‡*Postdoctoral Work-station, Shenzhen Academy of Aerospace Technology, Shenzhen, P.R. China*
§*Department of Automation and Computer-Aided Engineering, The Chinese University of Hong Kong, Hong Kong, P.R. China.*

(Received in Final Form: July 23, 2009. First published online: August 27, 2009)

SUMMARY

The technologies of autonomous rendezvous and robotic capturing of non-cooperative targets are very crucial for the future on-orbital service. In this paper, we proposed a method to achieve this aim. Three problems were addressed: the target recognition and pose (position and attitude) measurement based on the stereo vision, the guidance, navigation and control (GNC) of the chaser, and the coordinated plan and control of space robot (CP&C). The pose measurement algorithm includes image filtering, edge detection, line extraction, stereo match and pose computing, *et al*. Based on the measured values, a certain GNC algorithm was designed for the chaser to approach and rendezvous with the target. Then the CP&C algorithm, which is proved to be advantageous over the traditional separated method, was used to plan and track the trajectories of the base pose and the joint angle. At last, a 3D simulation system was developed to evaluate the proposed method. Simulation results verified the corresponding algorithms.

KEYWORDS: Space robot; Non-cooperative target; Rendezvous and dock; Autonomous capturing; Path planning.

1. Introduction

Robotic systems are expected to play an increasingly important role in future space activities. One broad area of application is in the servicing, construction, and maintenance of satellites and large space structures in orbit. Therefore, space robotic technologies have been emphasized by many countries.[1–6] Recently, the *Orbital Express* system, sponsored and led by the *Defense Advanced Research Projects Agency* (DARPA), validated on-orbit satellite servicing technologies.[4] The most remarkable mission was that a satellite autonomously rendezvoused with and captured another satellite in space, prolonging the way for future space servicing.

The autonomous rendezvous and capturing technologies, which have been successfully demonstrated by the Engineering Test Satellite VII (ETS-VII)[7] and orbital express,[8] are the keys of space robot for on-orbital servicing. In the demonstrations, a sub-satellite (target) was approached and successfully docked with by a main satellite (chaser). However, the targets were cooperative in the sense that they were equipped with transponders, reflectors, artificial markers that allowed friendly response to the chaser's sensors, as well as with dedicated grappling fixtures that allowed easy but secure capture by the end-effectors on the chaser. In contrast, the satellites already existing in orbit and requiring service are generally non-cooperative targets with no such features, i.e. neither any artificial patterns used for the cooperative measurement nor grappling fixtures applied for the capture, are mounted on the target.

Some organizations and individuals studied the issues about the capturing of non-cooperative targets, which is necessary for the future on-orbital servicing. Damaged, malfunctioned satellites or space debris are typical non-cooperative targets. DLR (i.e. German Space Agency) proposed the concept of the Experimental Servicing Satellite (ESS) for repairing and/or transferring the TV-SAT into a graveyard orbit.[9] The nozzle of the apogee motor has been identified as an adequate element/appendix to be captured. ESA (European Space Agency) has designed a satellite servicing system – RObotic GEostationary Orbit Restorer (ROGER), to clean up the geostationary orbit of switched-off satellites and debris, and transport it into a graveyard orbit.[10] Thienel *et al*.[11] presented a nonlinear approach for estimating the body rates of a non-cooperative target vehicle, and coupling this estimation to a tracking control scheme. Yoshida[12] and Nakanishi *et al*.[13] developed impedance control to capture a non-cooperative target.

However, few researchers considered the relative pose measurement, and the corresponding path planning and control method of space robot for capturing non-cooperative target. In fact, a complete capturing operation comprises three specific phases: the pre-impact phase, the impact phase, and the post-impact phase. Nenchev and Yoshida have proposed the detailed modelling of contact dynamics and the corresponding control after impact.[14] In this paper, aiming at the pre-impact phase of capturing a non-cooperative target, we investigated the general traits of spacecrafts, and proposed a method to autonomous rendezvous with and capture non-cooperative targets in space. Moreover, a simulation system is developed to verify the presented method.

The paper is organized as follows: Section 2 derives the kinematic and dynamic equations of the system. Sections 3

* Corresponding author. E-mail: wfxu@robotsat.com

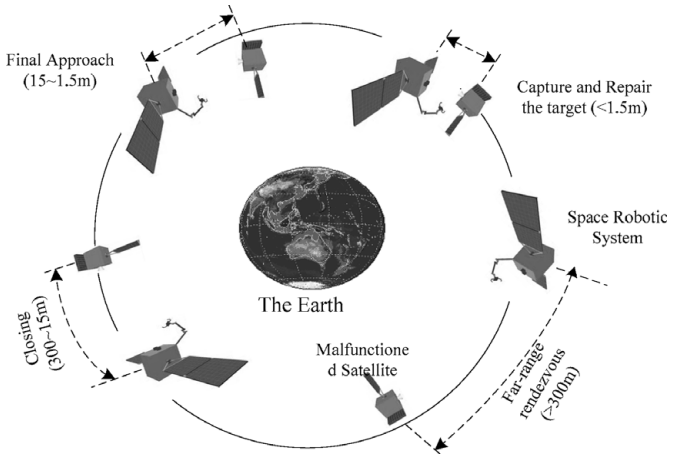

Fig. 1. A typical on-orbit servicing mission for non-cooperative target.

and 4 introduce the problem of the non-cooperative target recognition and relative pose measurement, respectively. Then, the autonomous path planning and control algorithms for approaching and capturing the target are proposed in Section 5. In Section 6, a 3D real-time simulation system is created and a typical case is studied. Section 7 is the discussion and conclusion of the work. The last section is the acknowledgements.

2. Modelling of the System

2.1. The on-orbital service for non-cooperative target

A typical on-orbit servicing mission is conducted in a series of operations, shown in Fig. 1. It mainly includes:[15] far range rendezvous, close range rendezvous (is usually divided into two subphases: closing and final approach), target capturing and repairing.

The major objective of the far range rendezvous, also called 'homing', is the reduction of trajectory dispersions, i.e. the achievement of position, velocity and angular rate conditions which are necessary for the initiation of the close range rendezvous operations. The closing phase is a preparatory phase leading to the final approach corridor. Its objectives are the reduction of the range to the target and the achievement of conditions allowing the acquisition of the final approach corridor. Then the chaser 'final approach' to achieve docking or berthing capture conditions in terms of positions and velocities and of relative attitude and angular rates. The last phase is that the manipulator captures the target and repairs it.

In this paper, we study the final approach and capture phases, which are very important for the on-orbital servicing.

2.2. The dynamic and kinematic modelling of the system

Major research achievements on space robot were collected by Xu and Kanade,[16] and were also reviewed by Moosavian and Papadopoulos recently.[17] Here, we model the space robotic system using Lagrangian method. The so-called inertial frame Σ_I is actually defined at the system's CM, i.e. its origin O_I is the same as the origin of Σ_{O1}. Then, the differential kinematic equation is determined as:

$$\begin{bmatrix} \boldsymbol{v}_e \\ \boldsymbol{\omega}_e \end{bmatrix} = \boldsymbol{J}_b \begin{bmatrix} \boldsymbol{v}_0 \\ \boldsymbol{\omega}_0 \end{bmatrix} + \boldsymbol{J}_m \dot{\boldsymbol{\Theta}}, \tag{1}$$

where, $\boldsymbol{J}_b$ and $\boldsymbol{J}_m$ are the Jacobian matrixes dependent on the base and the manipulator, respectively.

$$\boldsymbol{J}_b = \begin{pmatrix} \boldsymbol{E} & -\tilde{\boldsymbol{p}}_{0e} \\ \boldsymbol{O} & \boldsymbol{E} \end{pmatrix} \in \boldsymbol{R}^{6\times 6}, \quad \boldsymbol{p}_{0e} = \boldsymbol{p}_e - \boldsymbol{r}_0, \tag{2}$$

$$\boldsymbol{J}_m = \begin{bmatrix} \boldsymbol{k}_1 \times (\boldsymbol{p}_e - \boldsymbol{p}_1) & \dots & \boldsymbol{k}_n \times (\boldsymbol{p}_e - \boldsymbol{p}_n) \\ \boldsymbol{k}_1 & \dots & \boldsymbol{k}_n \end{bmatrix} \in \boldsymbol{R}^{6\times n}. \tag{3}$$

Operator $\tilde{\boldsymbol{r}}$ is the cross-product operator, i.e.

$$\text{if} \quad \boldsymbol{r} = \begin{bmatrix} r_x \\ r_y \\ r_z \end{bmatrix}, \text{ then } \quad \tilde{\boldsymbol{r}} = \begin{bmatrix} 0 & -r_z & r_y \\ r_z & 0 & -r_x \\ -r_y & r_x & 0 \end{bmatrix}. \tag{4}$$

Moreover, the dynamic equation of space robot is derived from the Lagrange function, and is generally expressed in the following form:[3]

$$\begin{bmatrix} \boldsymbol{H}_b & \boldsymbol{H}_{bm} \\ \boldsymbol{H}_{bm}^T & \boldsymbol{H}_m \end{bmatrix} \begin{bmatrix} \ddot{\boldsymbol{x}}_b \\ \ddot{\boldsymbol{\Theta}}_s \end{bmatrix} + \begin{bmatrix} \boldsymbol{c}_b \\ \boldsymbol{c}_m \end{bmatrix} = \begin{bmatrix} \boldsymbol{F}_b \\ \boldsymbol{\tau}_m \end{bmatrix}, \tag{5}$$

where $\boldsymbol{H}_b \in \boldsymbol{R}^{6\times 6}$: inertia matrix of the base; $\boldsymbol{H}_m \in \boldsymbol{R}^{n\times n}$: inertia matrix of the manipulator arm; $\boldsymbol{H}_{bm} \in \boldsymbol{R}^{6\times n}$: coupling inertia matrix of the base and manipulator; $\boldsymbol{c}_b \in \boldsymbol{R}^6$: velocity dependent nonlinear term for the base; $\boldsymbol{c}_m \in \boldsymbol{R}^6$: velocity dependent non-linear term for the arm; $\boldsymbol{F}_b \in \boldsymbol{R}^6$: force and torque on the centroid of the base; $\boldsymbol{\tau}_m \in \boldsymbol{R}^n$: torque on the manipulator joints.

3. The Problem of the Non-cooperative Target Recognition

3.1. The general features of the spacecraft to be recognized

According to the investigation of most satellites, it is found that one or more features as follows can be taken as the recognition objects and capture points:

(a) The target satellite itself: Since the shape of the target satellite's main body is usually cubical, polyhedral or cylindrical, it naturally can be imaged by optical sensors (such as CCD cameras) and recognized using advanced image processing algorithms. However, if the target is large, the optical sensors can not photograph it in the close range, limited by the FOV (field of view) of cameras. Moreover, it is difficult to design an end-effector which can grasp a large object. Therefore, the target main body is generally not considered as the recognizing and grasping object during final approach and capturing stages. To complete the whole on-orbit servicing tasks shown in Fig. 1, many sensors are required. Such as Orbital Express, the Autonomous Rendezvous and Capture Sensor System (ARCSS) consists of three imaging sensors (a narrow field of view camera, a

https://doi.org/10.1017/S0263574709990397 Published online by Cambridge University Press

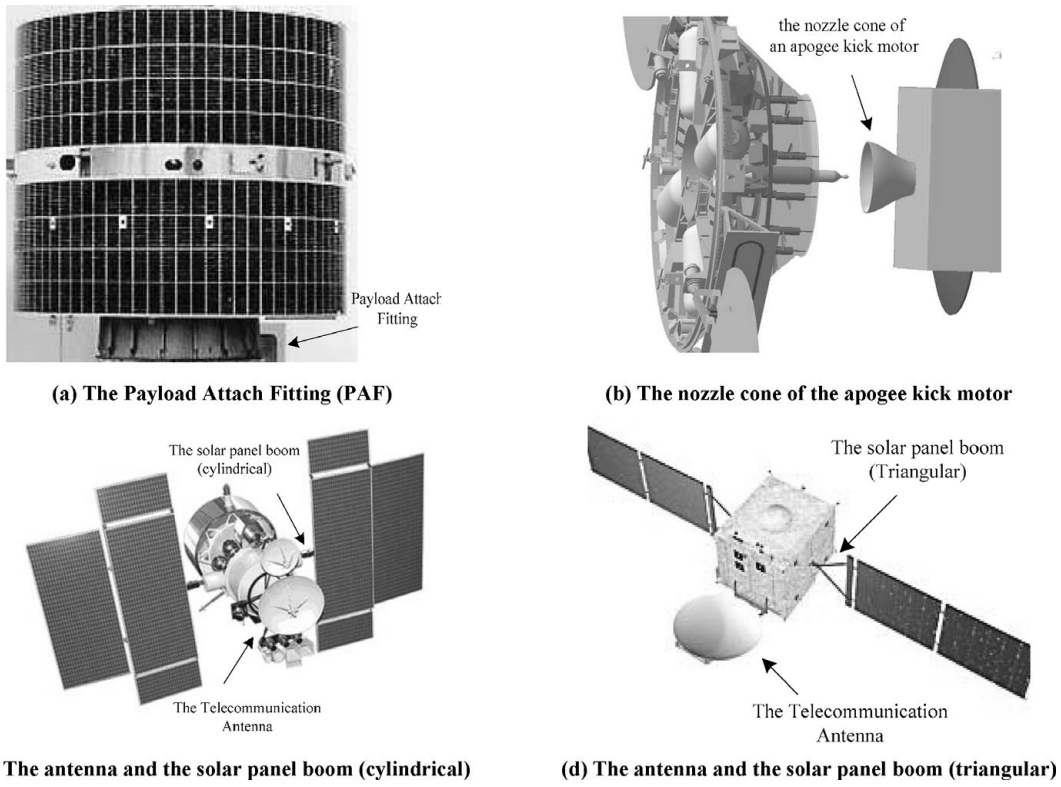

(a) The Payload Attach Fitting (PAF)

(b) The nozzle cone of the apogee kick motor

(c) The antenna and the solar panel boom (cylindrical)

(d) The antenna and the solar panel boom (triangular)

Fig. 2. The features on the satellite to be identified: (a) the payload attach fitting (PAF); (b) the nozzle cone of the apogee kick motor; (c) the antenna and the solar panel boom (cylindrical); (d) the antenna and the solar panel boom (triangular).

wide field of view camera and an infrared sensor), a precision laser rangefinder (cued by the imaging sensors, is used for mid range tracking), and Advanced Video Guidance Sensor (AVGS).[18] Here, we only consider the final approach and capturing stages; the design of measurement devices for the whole on-orbit servicing process is out of the range of this paper.

(b) The solar panel: most satellites have solar panels to supply the power for their subsystems. A solar panel is also of regular shape and can be used as the recognized object. But, the same reason as case (a), the sensors can not 'look' the whole panel when the distance is close.

(c) The payload attach fitting (PAF, see (a) of Fig. 2): among common features in the mechanical design of conventional satellites, the PAF is a good candidate to be grasped.[12] The PAF is a high-strength structure that is used to connect the satellite to the launch vehicle.

(d) The nozzle cone of an apogee kick motor (see (b) of Fig. 2): as another candidate grappling point, the nozzle cone of an apogee kick motor (engine) is promising. Geostationary satellites are commonly equipped with an apogee kick motor, the mounting base of which has high structural strength. Therefore, inserting a probe into the nozzle cone of the engine is also being studied.[9]

(e) The solar panel or the antenna booms (or supports) (see (c), (d) of Fig. 2): the solar panel or the antenna booms (or supports) are typically cylindrical or triangular. The diameter or the thickness is generally not greater than 30 mm. Here, the booms are thought as the most appropriate recognized object and grasping point of a non-cooperative satellite.

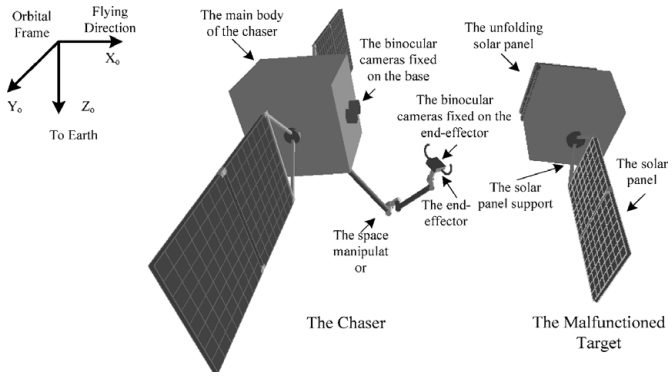

Fig. 3. The space robotic system and the non-cooperative target.

In this paper, taking a non-cooperative target with triangular solar panel support as the example, we proposed a method based on stereo vision to measure the relative pose of the target, and an autonomous path planning and coordinated control approaches of the space robot to capture the target.

3.2. The space robotic system designed to service a non-cooperative target

The target to be serviced is assumed a malfunctioned satellite, one of whose solar panels is unfolded. The designed space robotic system (the chaser spacecraft) used for the on-orbital servicing mission is shown as Fig. 3. It is composed of a carrier spacecraft (called *Space Base* or *Base*) and a PUMA-type manipulator (called *Space Manipulator*). There are two sets of stereo cameras (4 cameras in total) on the chaser for the pose measurement and target inspection. The binocular

https://doi.org/10.1017/S0263574709990397 Published online by Cambridge University Press

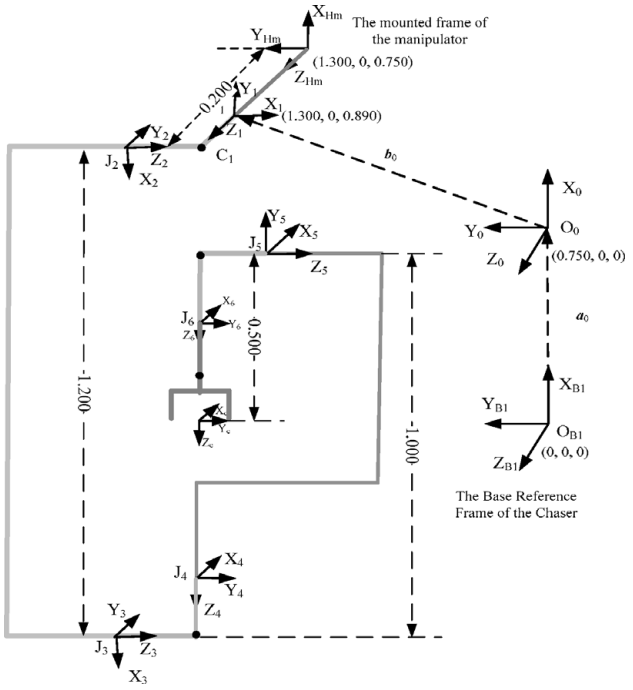

Fig. 4. The body-fixed frames of the space robotic system.

cameras mounted on the base (called *Base Stereo Cameras*) are utilized to measure the relative pose of the target, and the binocular cameras fixed on the end-effector (called *End-effector Binocular Cameras*) are used to inspect the devices on the chaser or the target. The end-effector is a two-finger gripper used to grasp the target.

The frames fixed on the multi-body system are defined as Fig. 4 (when the joint angles are all zeros), where Z_i is the direction of J_i, vectors $\boldsymbol{a}_i, \boldsymbol{b}_i \in \boldsymbol{R}^3$ and are $\boldsymbol{I}_i \in \boldsymbol{R}^3$ defined as ref. [3]. Table I lists the dimensions and mass properties of the bodies (*Sat* and B_i stand for the satellite and the ith body, respectively). The left and right cameras of the base binocular cameras are respectively fixed at (1.500, −0.180, 0) and (1.500, 0.180, 0) of Σ_{B1} — the body reference frames on the chaser. And the rendezvous reference frame Σ_{R1} (is chosen as the world frame of the base stereo vision, denoted by Σ_W) of the chaser lies at (1.500, 0, 0) of Σ_{B1}. The two cameras of the end-effector stereo vision are mounted at (0.080, −0.080, −0.100) and (0.080, 0.080, −0.100) of Σ_E. The units of the coordinates are 'm'.

3.3. The 3D reconstruction based on binocular stereo vision

The pin-hole model is the most used projection model of the camera. Assume a point P, whose coordinates with respect to Σ_W are denoted by ${}^W\boldsymbol{P} = [X_W,\ Y_W,\ Z_W]^T$, will project on the image plane with coordinates (u, v), then the following relationship exists:

$$\lambda \begin{bmatrix} u \\ v \\ 1 \end{bmatrix} = \boldsymbol{C} \begin{bmatrix} X_W \\ Y_W \\ Z_W \\ 1 \end{bmatrix}, \tag{6}$$

where $\lambda \neq 0$ is a constant, $\boldsymbol{C}$ is the projection transform matrix, which determined by the intrinsic parameters and the extrinsic parameters of the camera. Equation (6) is the bridge between the point in 3D space and its projection on the 2D image plane. For the practical application, the process is in reverse, i.e. the 3D coordinates (X_W, Y_W, Z_W) are required to be measured according to the 2D coordinates (u, v) extracted from the camera images. However, known from Eq. (6), one point on the image plane actually denotes a line (infinite points) in 3D space. That is to say, monocular camera cannot measure the 3D position of the target, if there is not any prior knowledge. This is the reason for the cooperative measurement, where artificial features (the geometrical dimensions and relative position between them are known) are designed for the monocular vision.

The binocular vision is very useful to deal with many practical problems of the autonomous robots, such as the point-to-trajectory positioning and tracking tasks in uncalibrated environments.[19–20] The key for the application of the stereo vision is 3D reconstruction. It is assumed that the coordinates of the ith feature point P_i are ${}^W\boldsymbol{P}_i = [X_{Wi}\ Y_{Wi}\ Z_{Wi}]^T$, and the corresponding image coordinates in the left image plane and right image plane are respectively denoted as $\boldsymbol{p}_{Li} = [u_{Li}\ v_{Li}]^T$ and $\boldsymbol{p}_{Ri} = [u_{Ri}\ v_{Ri}]^T$.

Table I. The mass properties of the space robotic system.

		Sat	B_1	B_2	B_3	B_4	B_5	B_6
Mass (kg)		1500	20.1	17.5	20.1	17.0	20.1	11.9
${}^i\boldsymbol{a}_i$/m		0.750	0	0.600	0	0	0	0
		0	0	0	0	0.0843	0	0
		0	0.060	−0.0825	0.060	−0.440	−0.060	0.300
${}^i\boldsymbol{b}_i$/m		0.550	−0.060	0.600	−0.060	0	0	0
		0	0	0	0	−0.0243	−0.060	0
		0.890	0	0.0825	0	−0.500	0	0.140
${}^i\boldsymbol{I}_i$ (kg.m^2)	I_{xx}	490	0.082	0.044	0.2032	1.2329	0.2265	0.2122
	I_{yy}	520	0.180	2.2872	0.2265	1.0686	0.2032	0.2096
	I_{zz}	510	0.160	2.2824	0.130	0.125	0.1593	0.2079
	I_{xy}	−1.341	0	0	0	0	0	0
	I_{xz}	1.68	−0.012	0	−0.0100	0	0	0
	I_{yz}	−1.55	0	0	0	0.2024	0.0050	0

https://doi.org/10.1017/S0263574709990397 Published online by Cambridge University Press

According to Eq. (6), the relationships correspond to the left and right cameras are as follows:[20]

$$\begin{bmatrix} \lambda_L u_{L_i} \\ \lambda_L v_{Li} \\ \lambda_L \end{bmatrix} = \boldsymbol{C}_L \begin{bmatrix} X_{wi} \\ Y_{wi} \\ Z_{wi} \\ 1 \end{bmatrix} = \begin{bmatrix} 1 & \alpha_1 & \alpha_2 & \alpha_3 \\ \alpha_4 & \alpha_5 & \alpha_6 & \alpha_7 \\ \alpha_8 & \alpha_9 & \alpha_{10} & \alpha_{11} \end{bmatrix} \begin{bmatrix} X_{wi} \\ Y_{wi} \\ Z_{wi} \\ 1 \end{bmatrix}, \tag{7}$$

$$\begin{bmatrix} \lambda_R u_{Ri} \\ \lambda_R v_{Ri} \\ \lambda_R \end{bmatrix} = \boldsymbol{C}_R \begin{bmatrix} X_{wi} \\ Y_{wi} \\ Z_{wi} \\ 1 \end{bmatrix} = \begin{bmatrix} 1 & \beta_1 & \beta_2 & \beta_3 \\ \beta_4 & \beta_5 & \beta_6 & \beta_7 \\ \beta_8 & \beta_9 & \beta_{10} & \beta_{11} \end{bmatrix} \begin{bmatrix} X_{wi} \\ Y_{wi} \\ Z_{wi} \\ 1 \end{bmatrix}, \tag{8}$$

where $\boldsymbol{C}_L$ and $\boldsymbol{C}_R$ are the projection transform matrixes of the left and right cameras respectively, and α_i,β_i are the elements of $\boldsymbol{C}_L$ and $\boldsymbol{C}_R$. In the practice, $\boldsymbol{C}_L$ and $\boldsymbol{C}_R$ can be calibrated beforehand. The calibration methods are widely studied and the readers can refer to.[21,22]

Equations (7) and (8) are simplified as follows

$$\begin{bmatrix} 1-\alpha_8 u_{Li} & \alpha_1-\alpha_9 u_{Li} & \alpha_2-\alpha_{10} u_{Li} \\ \alpha_4-\alpha_8 v_{Li} & \alpha_5-\alpha_9 v_{Li} & \alpha_6-\alpha_{10} v_{Li} \\ 1-\beta_8 u_{Ri} & \beta_1-\beta_9 u_{Ri} & \beta_2-\beta_{10} u_{Ri} \\ \beta_4-\beta_8 v_{Ri} & \beta_5-\beta_9 v_{Ri} & \beta_6-\beta_{10} v_{Ri} \end{bmatrix} \begin{bmatrix} X_{wi} \\ Y_{wi} \\ Z_{wi} \end{bmatrix} = \begin{bmatrix} \alpha_{11} u_{Li}-\alpha_3 \\ \alpha_{11} v_{Li}-\alpha_7 \\ \beta_{11} u_{Ri}-\beta_3 \\ \beta_{11} v_{Ri}-\beta_7 \end{bmatrix}. \tag{9}$$

Equation (9) can be written into matrix form,

$$\boldsymbol{K} \cdot {}^W\boldsymbol{P}_i = \boldsymbol{U}. \tag{10}$$

There are four equations but only three unknowns in Eq. (10). So the 3D coordinates of point P_i can be solved using the least square method, i.e.

$${}^W\boldsymbol{P}_i = (\boldsymbol{K}^T\boldsymbol{K})^{-1}\boldsymbol{K}^T\boldsymbol{U}. \tag{11}$$

Equation (11) is the principle of 3D reconstruction based on binocular stereo vision. That is to say, the 3D coordinates of Point P_i can be 'reconstructed' from its 2D image coordinates of the two cameras. The key is that the two cameras observe the same point and extract the corresponding image feature points. If more than three points are 3D reconstructed, some target fixed frames (such as Σ_{R2} and Σ_{Cap}) can be determined.

4. The Pose Measurement of the Non-cooperative Target

4.1. Main procedure

As the discussion of Section 3.1, the triangle solar panel support is chosen as the recognized object. In fact, when the distance between the chaser and the target is sufficiently far, the main body can be photographed and the approach based on stereo vision is applicable to recognize the vertexes of the main body's contour. Then a reference frame (temporarily denoted by Σ_R) fixed on the target can be constructed using the recognized feature points. And the pose of Σ_R with respect to the vision frame can be measured. This concept is used as a backup way when the panel support is not in the view but the stereo cameras observe the main body of the target. However, the main body itself cannot be 'grasped' by a traditional end-effector. Therefore, the solar panel support should be taken as the recognized and grasped object in close distance. The main steps include *image grabbing*, *image smoothing*, *edge detection*, *line extraction*, *recognition of the solar panel support*, *determining of the feature points*, *stereo match* and *calculating the target pose*. A practical example is given to illuminate the algorithm in details.

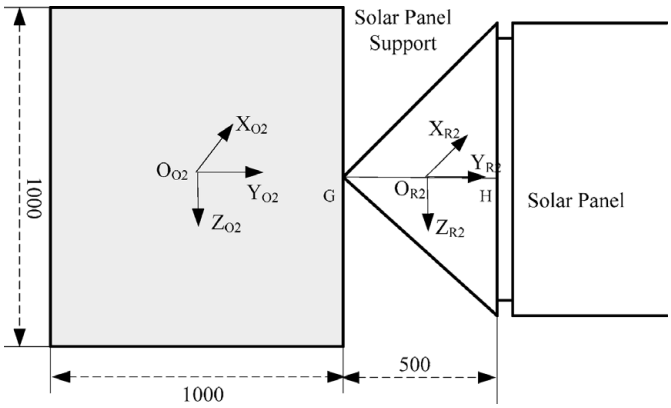

Fig. 5. The geometry of the target satellite.

4.2. An example for the pose measurement of the non-cooperative target

4.2.1. The emulated image grabbing. Not loss of generality, the main body of the target is assumed to be a $1000 \times 1000 \times 1000\,\text{mm}^3$ cube, and the CM frame lies at the geometry centre of the cube. The rendezvous reference frame on the target Σ_{R2} is defined as Fig. 5; its origin is the centre of height *GH*. The coordinates of O_{R2} is (0, 0.750, 0) in Σ_{O2}.

The initial position of the chaser's CM relative to the orbital frame of the target is

$$\boldsymbol{r}_{c0} = [-5.500\,\text{m},\ 0.150\,\text{m},\ -0.300\,\text{m}]^T. \tag{12}$$

The attitudes of the chaser and the target are respectively

$$\boldsymbol{\Psi}_{c0} = [-2^\circ, 3^\circ, -4^\circ]^T, \tag{13}$$

$$\boldsymbol{\Psi}_{t0} = [5^\circ, -4^\circ, 8^\circ]^T. \tag{14}$$

The joint angles of the manipulator are

$$\boldsymbol{\Theta}_0 = [0^\circ, -36^\circ, 39^\circ, 180^\circ, -131^\circ, 133^\circ]^T. \tag{15}$$

In order to theoretically verify the proposed method, the technology of the computer image and graph is used to generate the emulated images of the binocular cameras. First, the geometry models of the chaser (including the base and the

https://doi.org/10.1017/S0263574709990397 Published online by Cambridge University Press

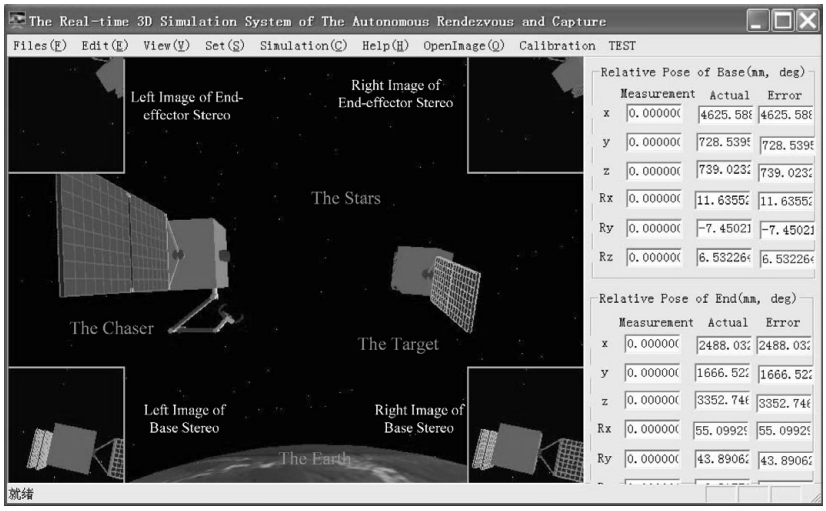

Fig. 6. The 3D geometry model created using OpenGL.

manipulator), the target and the background (the earth, the stars and the orbital environment) are created using OpenGL, a software interface to graphics hardware, according to their geometry parameters, positions and attitudes. OpenGL consists of about 120 distinct commands, which we can use to specify the objects and operations needed to produce interactive 3D applications.[23]

It should be pointed out that, the illumination condition and the star map are modelled simply. The positions and the luminance of the stars are possibly not the same as the real case, and the earth albedo is not considered. The complete modelling of the orbital environment will be considered in the future research. The model correspond to the position and attitude defined by Eqs. (12)–(15) is shown in Fig. 6.

Virtual cameras are created in OpenGL to emulate the imaging of the real cameras, according to their optical parameters (CCD size, field of view, *et al.*) and positions where they are mounted. The virtual camera setup is commonly done with gluPerspective and gluLookAt functions, determines what is visible on screen (i.e. the view frustum). The real cameras of the base stereo vision are black and white cameras with 36° FOV angles and 512×512 pixels CCD. Figure 7 shows the generated images of the left camera corresponding to the state defined by Eqs. (12)–(15).

In order to reflect the operation condition as real as possible, the main noise sources should be added to the modelling and simulation system. According to the investigation of physical vision system, there exist at least the following noises: (a) thermal noise (also called dark current noise), arising from thermal energy within the silicon lattice comprising the CCD. As the integration time T increases, the number of thermal electrons increases. (b) On-chip electronic noise, originating in the process of reading the signal from the sensor, in this case through the field effect transistor (FET) of a CCD chip; (c) amplifier noise, which is additive, Gaussian and independent of the signal. In modern well-designed electronics, amplifier noise is generally negligible. (d) Quantization noise, which is inherent in the amplitude quantization process and occurs in the analogue-to-digital converter (ADC). The noise is additive and independent of the signal when the number of levels $L >= 16$ (i.e. 4 bits

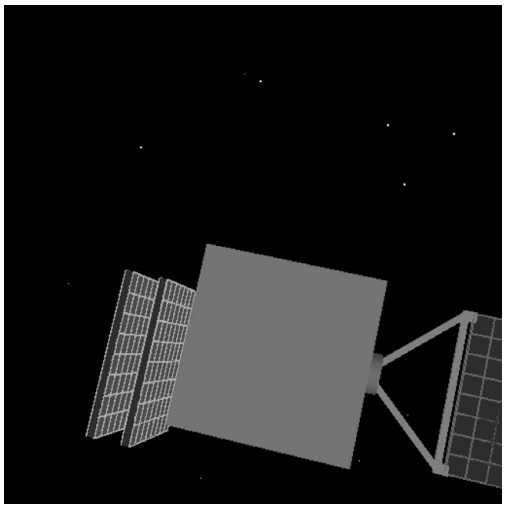

Fig. 7. The emulated left image (512×512).

binary number). It has an approximately uniform distribution. Quantization noise can usually be ignored when using high-bit ADC ($B > 8$). Then the total noise can be modelled as independent additive white Gaussian noise, i.e. the noisy image is

$$I_0(u, v) = I(u, v) + n(u, v), \tag{16}$$

where, $I_0(u, v)$ denotes the pixel value of a noise image at (u, v), $I(u, v)$ denotes the ideal clean image, and $n(u, v)$ is the noise, whose mean and variance values are assumed as

$$\begin{cases} \bar{n} = 20 \\ \sigma_n = 400 \end{cases}. \tag{17}$$

The left image, to which added Gaussian white noises of mean $\bar{n}$ and variance σ_n, is shown as Fig. 8 (The right image is not shown). These noisy images, used to model the sampled images of real cameras, will be processed in the following section. Limiting to the length of the paper, only the processing results of the left image are given in the following parts, and those of the right image are similar.

https://doi.org/10.1017/S0263574709990397 Published online by Cambridge University Press

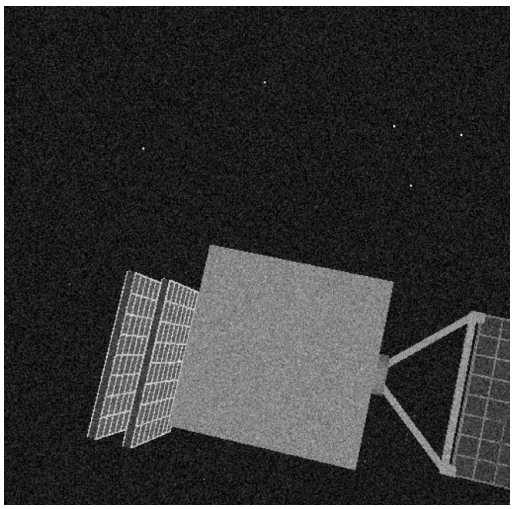

Fig. 8. The noisy image of the left camera.

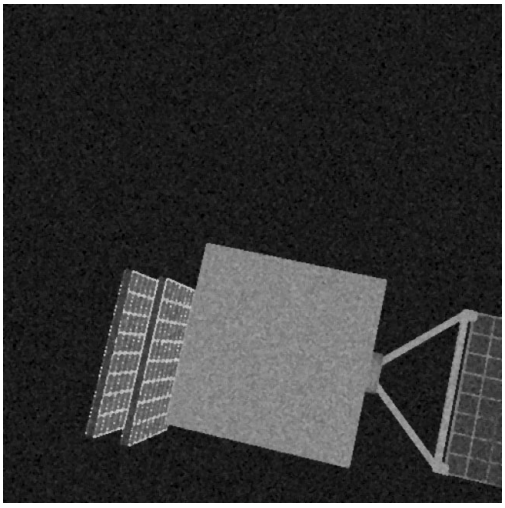

Fig. 9. The left image after median filtering.

4.2.2. Image filtering. Noise will get introduced into the images via any electrical system used for storage, transmission and/or processing. Then we will apply some techniques to improve the images for the specific application. Median filtering is a simple and very effective noise removal filtering process. Its performance is particularly good for removing shot noise. Shot noise consists of strong spike-like isolated values. When performing median filtering, each pixel is determined by the median value of all pixels in a selected neighbourhood (mask, template and window). The median value m of a population (set of pixels in a neighbourhood) is that value in which half of the population has smaller values than m, and the other half has larger values than m. The filtered images of the noised left camera are shown as Fig. 9 (The original image is shown in Fig. 8).

4.2.3. Edge detection. The Canny edge detection algorithm is known to many as the optimal edge detector. Here we use it to detect the edge of the filtered left and right images. A list of criteria is used.[24] The first and most obvious is low-error rate. It is important that edges occurring in images should not be missed and that there be no responses to non-edges. The second criterion is that the edge points be

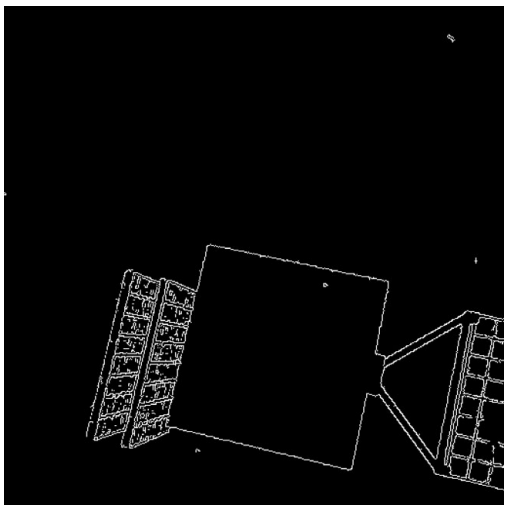

Fig. 10. The detected edges from using the Canny algorithm.

well localized. In other words, the distance between the edge pixels as found by the detector and the actual edge is to be at a minimum. A third criterion is to have only one response to a single edge. This was implemented because the first two were not substantial enough to completely eliminate the possibility of multiple responses to an edge. Based on these criteria, the canny edge detector first smoothes the image to eliminate and noise. It then finds the image gradient to highlight regions with high spatial derivatives. The algorithm then tracks along these regions and suppresses any pixel that is not at the maximum (non-maximum suppression). The gradient array is now further reduced by hysteresis. Hysteresis is used to track along the remaining pixels that have not been suppressed. Hysteresis uses two thresholds and if the magnitude is below the first threshold, it is set to zero (made a non-edge). If the magnitude is above the high threshold, it is made an edge. And if the magnitude is between the two thresholds, then it is set to zero unless there is a path from this pixel to a pixel with a gradient above the second threshold. The detected edges of the left image are shown in Fig. 10.

4.2.4. The recognition of the solar panel support. After the processing of Canny algorithm, we obtain the binary image images containing the edge information. In order to recognize the solar panel support, the Hough Transform is used to extract the lines in the binary image. It is reported that Hough Transform performs well in line detection,[24] especially for an object that is incompletely delineated or contaminated by noise. The concept of Hough Transform is to transfer an object from image space to parameter space using suitable mathematic functions. Those functions should be able to describe the geometric properties of an object, such as straight-lines, circles, ellipses, etc. Due to their distinctness, usefulness and generality for object reconstruction, straight lines will be considered in this investigation. According to the Hough Transform, each point of interest is transformed to a sinusoidal curve in the angle-distance parameter space. If a group of points belong to a straight-line in an image, their corresponding sinusoidal curves will be intersected at a point in the parameter space. In order to detect the

https://doi.org/10.1017/S0263574709990397 Published online by Cambridge University Press

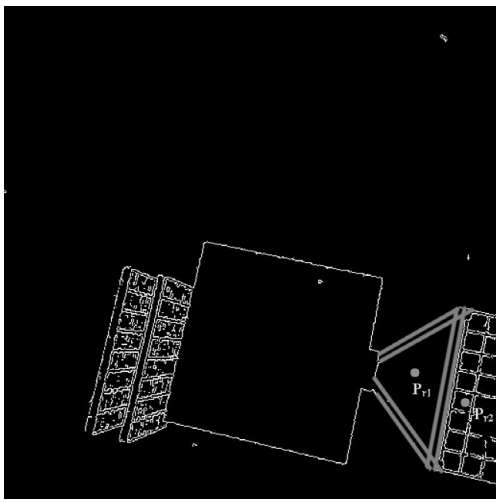

Fig. 11. The recognized solar panel support in the left image.

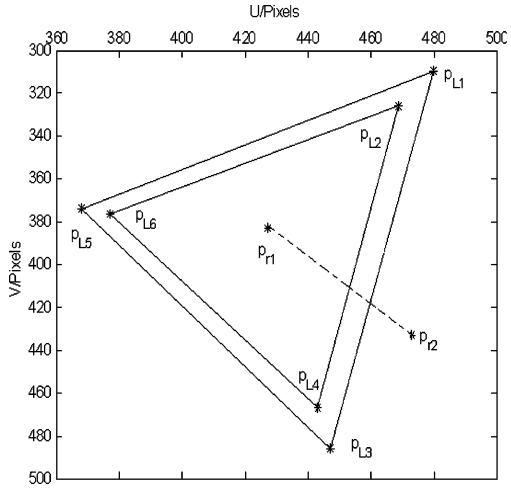

Fig. 12. The extraction of the point feature from the left image.

intersection point in the parameter space, a 2D accumulative array is necessary. When two sinusoidal curves intersect at a point, the counting value in the accumulative array is increased by one. The detection of straight-line in an image space is changed to detect peaks in the parameter space.

However, many lines will be extracted, such as the outlines of the satellite, the grid of the solar array, the solar panel support, *et al*. Then some algorithms are required to recognize those lines belong to the solar panel support. Initially, two reference points (P_{r1} and P_{r2}) on the images are chosen to assistantly recognize these lines, through the tele-operation link. Points P_{r1} and P_{r2} are set by mouse click on the downstream images from the ground–space tele-operation. This operation is conducted only once. Then the new reference points are estimated and tracked on real time. No special constraints on the selection of Points P_{r1} and P_{r2}, except that P_{r1} lies inside the triangular and P_{r2} lies on the solar panel. Then the two lines of the right edge($P_{L1}P_{L3}$, $P_{L2}P_{L4}$) of the triangle can be determined by Points P_{r1} and P_{r2}. And the two upper lines (of the upper edge, i.e. $P_{L1}P_{L5}$ and P_{L2} P_{L6}) are recognized according to Points P_{r1}, P_{r2} and the two right lines. At last, the two lower lines (of the lower edge, i.e. $P_{L3}P_{L5}$ and $P_{L4}P_{L6}$) are determined. After the six lines are determined, the triangular solar panel support is recognized. These processed are shown as Figs. 11 and 12. The corresponding intersection points are extracted according to the intersection point equations of two lines.

4.2.5. The calculation of the target pose. In this paper, the virtual cameras are calibrated according to the emulated calibration images, 7 × 7 circular marker arrays. Then the 3D coordinates of the six feature points can be determined according to the extracted 2D features, and the 3D reconstruction Eq. (11).

After the six feature points are extracted, the 'the rendezvous reference frame on the target' Σ_{R2} and the 'capture point frame on the target' Σ_{Cap} can be defined, which is illuminated in Fig. 13.

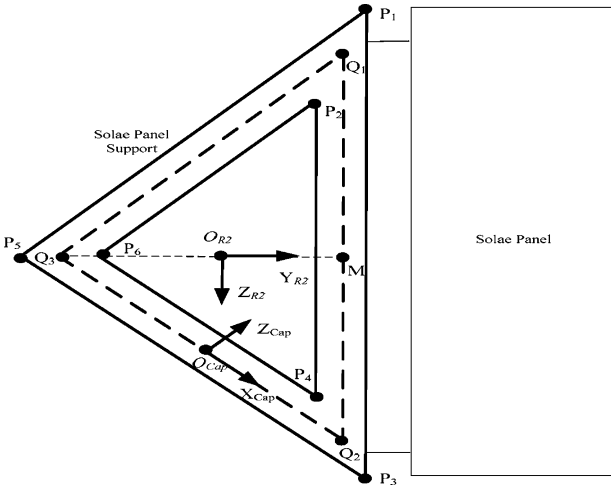

Fig. 13. The definitions of the target frame and the capture frame.

First, the three points ($\boldsymbol{Q}_1$–$\boldsymbol{Q}_3$) denoting the centre triangle of the support are determined, i.e.

$$^{W}\boldsymbol{Q}_1 = \frac{^{W}\boldsymbol{P}_1 + {}^{W}\boldsymbol{P}_2}{2}, \tag{18}$$

$$^{W}\boldsymbol{Q}_2 = \frac{^{W}\boldsymbol{P}_3 + {}^{W}\boldsymbol{P}_4}{2}, \tag{19}$$

$$^{W}\boldsymbol{Q}_3 = \frac{^{W}\boldsymbol{P}_5 + {}^{W}\boldsymbol{P}_6}{2}. \tag{20}$$

Then

$$^{W}\boldsymbol{M} = \frac{^{W}\boldsymbol{Q}_1 + {}^{W}\boldsymbol{Q}_2}{2}. \tag{21}$$

And the origin of Σ_{R2} is

$$\boldsymbol{r}_{R2} = {}^{W}\boldsymbol{O}_t = \frac{^{W}\boldsymbol{Q}_3 + {}^{W}\boldsymbol{M}}{2}. \tag{22}$$

The X-axis is a unit vector (vector $\boldsymbol{n}_{R2}$), which is perpendicular to the plane $Q_1Q_2Q_3$, i.e.

$$\boldsymbol{n}_{R2} = \frac{\boldsymbol{Q}_3\boldsymbol{Q}_1 \times \boldsymbol{Q}_3\boldsymbol{Q}_2}{\|\boldsymbol{Q}_3\boldsymbol{Q}_1 \times \boldsymbol{Q}_3\boldsymbol{Q}_2\|}. \tag{23}$$

https://doi.org/10.1017/S0263574709990397 Published online by Cambridge University Press

The Y-axis is defined as a vector (vector $\boldsymbol{o}_{R2}$) along vector $\boldsymbol{Q}_3\boldsymbol{M}$, i.e.

$$\boldsymbol{o}_{R2} = \frac{\boldsymbol{Q}_3\boldsymbol{M}}{\|\boldsymbol{Q}_3\boldsymbol{M}\|}. \tag{24}$$

Then Z-axis determined according to the right-hand rule, i.e.

$$\boldsymbol{a}_{R2} = \boldsymbol{n}_{R2} \times \boldsymbol{o}_{R2}. \tag{25}$$

The rotation transform axis from Σ_{R1} to Σ_{R2} is

$$^{R1}\boldsymbol{A}_{R2} = [\boldsymbol{n}_{R2}\ \boldsymbol{o}_{R2}\ \boldsymbol{a}_{R2}]. \tag{26}$$

Similarly, the capture frame is defined by the following equations:

$$\boldsymbol{r}_{\text{Cap}} = \boldsymbol{O}_{\text{Cap}} = \frac{\boldsymbol{Q}_3 + \boldsymbol{Q}_2}{2}, \tag{27}$$

$$\boldsymbol{n}_{\text{Cap}} = \frac{\boldsymbol{Q}_3\boldsymbol{Q}_2}{\|\boldsymbol{Q}_3\boldsymbol{Q}_2\|}, \tag{28}$$

$$\boldsymbol{o}_{\text{Cap}} = \boldsymbol{n}_{R2}, \tag{29}$$

$$\boldsymbol{a}_{\text{Cap}} = \boldsymbol{n}_{\text{Cap}} \times \boldsymbol{o}_{\text{Cap}}, \tag{30}$$

$$^{R1}\boldsymbol{A}_{\text{Cap}} = [\boldsymbol{n}_{\text{Cap}}\ \boldsymbol{o}_{\text{Cap}}\ \boldsymbol{a}_{\text{Cap}}]. \tag{31}$$

Therefore, the attitude angles (Z-Y-X Euler angles) are calculated from the attitude matrix. For the conditions given as Eqs. (12)–(15), the theory poses of the target and the capture frame with respect to the world frame are respectively:

$$\begin{cases} ^{R1}\boldsymbol{r}_{R2} = [4.6256\ \ 0.72850.7390]^T \\ ^{R1}\boldsymbol{\Psi}_{R2} = [6.5323\ \ -7.4502\ \ 11.6355]^T \end{cases}, \tag{32}$$

$$\begin{cases} ^{R1}\boldsymbol{r}_{\text{Cap}} = [4.6024\ \ 0.6802\ \ 0.9576]^T \\ ^{R1}\boldsymbol{\Psi}_{\text{Cap}} = [106.5197\ \ -52.9836\ \ 167.5625]^T \end{cases}. \tag{33}$$

The proposed algorithm is applied to measure these poses and the results are

$$\begin{cases} ^{R1}\hat{\boldsymbol{r}}_{R2} = [4.6372\ \ 0.7348\ \ 0.7475]^T \\ ^{R1}\hat{\boldsymbol{\Psi}}_{R2} = [7.7288\ \ -8.6849\ \ 11.6452]^T \end{cases}, \tag{34}$$

$$\begin{cases} ^{R1}\hat{\boldsymbol{r}}_{\text{Cap}} = [4.6058\ \ 0.6859\ \ 0.9627]^T \\ ^{R1}\hat{\boldsymbol{\Psi}}_{\text{Cap}} = [109.2621\ \ -52.7560\ \ 165.6346]^T \end{cases}. \tag{35}$$

The measure errors are respectively as

$$\begin{cases} ^{R1}\boldsymbol{r}_{R2} - ^{R1}\hat{\boldsymbol{r}}_{R2} = [-0.0116\ \ -0.0063\ \ -0.0085]^T \\ ^{R1}\boldsymbol{\Psi}_{R2} - ^{R1}\hat{\boldsymbol{\Psi}}_{R2} = [-1.1965\ \ 1.2347\ \ -0.0097]^T \end{cases}, \tag{36}$$

$$\begin{cases} ^{R1}\boldsymbol{r}_{\text{Cap}} - ^{R1}\hat{\boldsymbol{r}}_{\text{Cap}} = [-0.0034\ \ -0.0057\ \ -0.0051]^T \\ ^{R1}\boldsymbol{\Psi}_{\text{Cap}} - ^{R1}\hat{\boldsymbol{\Psi}}_{\text{Cap}} = [-2.7424\ \ -0.2276\ \ 1.9279]^T \end{cases}. \tag{37}$$

5. The Planning and Control of the Space Robotic System

5.1. The guidance, navigation and control of the chaser

The chaser is controlled to approach and rendezvous with the target with a desired pose for the space manipulator to easily capture the target. During the approach, the manipulator keeps the fixed configuration and not generates disturbance on the base, i.e. the traditional navigation, guidance and control method can be used. The control loops for attitude and trajectory control include the sensors for position and attitude measurement, the GNC functions, and the thrusters and other actuator for attitude and position control.[15] Here, the 'rendezvous sensors' are actually the 'base stereo cameras', which measure the relative pose of the target. The measurement values are then used by the navigation function, consisting of a Kalman filter, which processes the various information of attitude (gyros, updated by Sun, Earth and/or star sensors) and pose (base stereo vision) and propagates the vehicle state in position and attitude by using the knowledge of the dynamic behaviour and information on the actual thrust commands. The guidance function defines the set values for the nominal evolution of the spacecraft state, i.e. the references for the control of position, velocities, attitude and angular rates at each point in time. The control function produces the force and torque commands necessary to achieve the desired corrections in attitude and trajectory and to ensure stability of the vehicle. The thruster management function transforms the torque and force commands into 'on/off' commands for the individual thrusters.

For the final approach, the trajectory is straight-line reference trajectory. When the chaser approaches close to the desired pose with respect to the target, the space manipulator is driven to capture the target. During the operation of the manipulator, the coordinated plan and control (CP&C) strategy of the base and the manipulator is used to control the base and the manipulator at the same time. The CP&C concept will be introduced in Section 5.3.

5.2. The path planning of the space manipulator

As discussed above, the binocular cameras of the end-effector are only used for the visual inspection (the distance is too near to satisfy the conditions of the stereo measurement). Therefore, the pose measurement of the base stereo vision is also used for the path planning of the manipulator, by transforming the measurement of the capture point's pose relative to the base to that with respect to the end-effector. Firstly, the end-effector's pose relative to the base is calculated using the direct kinematic equation of the space manipulator, according to the current joint angles, i.e.

$$^{O_1}\boldsymbol{p}_e = {}^0\boldsymbol{b}_0 + \sum_{k=1}^{n}\left({}^0\boldsymbol{a}_k + {}^0\boldsymbol{b}_k\right) = \boldsymbol{g}_m(\boldsymbol{\Theta}), \tag{38}$$

$$^0\boldsymbol{A}_e = {}^0\boldsymbol{A}_1 \cdot \cdots \cdot {}^{n-1}\boldsymbol{A}_n = \boldsymbol{f}_m(\boldsymbol{\Theta}). \tag{39}$$

https://doi.org/10.1017/S0263574709990397 Published online by Cambridge University Press

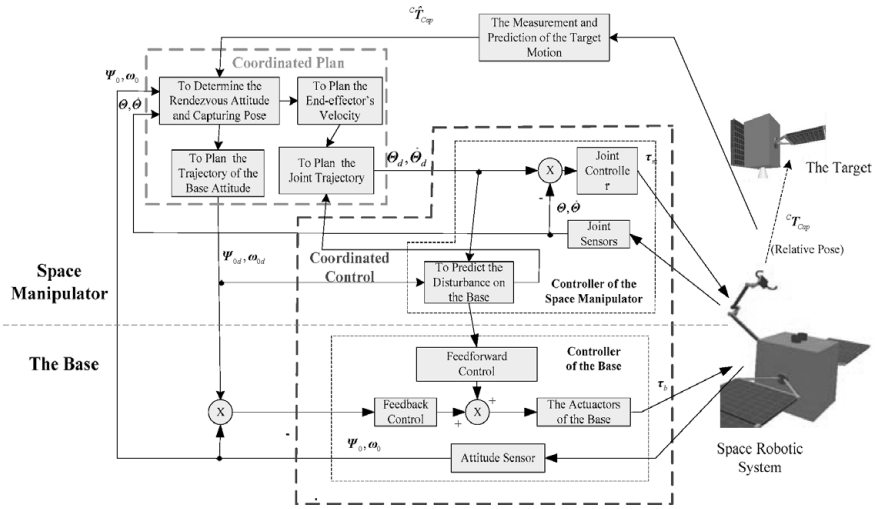

Fig. 14. The basic concept of the coordinated planning and control method for capturing a moving target.

Equations (38) and (39), showing that the pose of the end-effector relative to the base is independent on the base attitude, can be written as

$$^{0}\boldsymbol{T}_{e} = \boldsymbol{f}(\boldsymbol{\Theta}), \tag{40}$$

where $^{\circ}\boldsymbol{T}_{e}$ is the homologous transformation matrix of frame Σ_E with respect to frame Σ, i.e.

$$^{0}\boldsymbol{T}_{e} = \begin{bmatrix} ^{0}\boldsymbol{A}_{e} & ^{0}\boldsymbol{p}_{e} \\ \boldsymbol{O} & 1 \end{bmatrix}. \tag{41}$$

Equation (40) is actually the conventional position-level kinematic equation of the manipulator. Then the capture point's pose relative to the end-effector is calculated by

$$^{e}\boldsymbol{T}_{\mathrm{Cap}} = {}^{e}\boldsymbol{T}_{0} \cdot {}^{0}\boldsymbol{T}_{R1} \cdot {}^{R1}\hat{\boldsymbol{T}}_{\mathrm{Cap}}, \tag{42}$$

where

$$^{e}\boldsymbol{T}_{0} = \left({}^{0}\boldsymbol{T}_{e}\right)^{-1}. \tag{43}$$

And $^{0}\boldsymbol{T}_{R1}$ is the homologous transformation matrix from the base to the chaser rendezvous frame. Since the two frames are fixed on the base, $^{0}\boldsymbol{T}_{R1}$ is a constant matrix given as

$$^{0}\boldsymbol{T}_{R1} = \begin{bmatrix} 1 & 0 & 0 & 0.75 \\ 0 & 1 & 0 & 0 \\ 0 & 0 & 1 & 0 \\ 0 & 0 & 0 & 1 \end{bmatrix}. \tag{44}$$

Matrix $^{R1}\hat{\boldsymbol{T}}_{\mathrm{Cap}}$, the homologous transformation matrix of the capture point frame with respect to the chaser rendezvous frame, is directly measured by the binocular stereo vision of the base.

According to Eq. (42), the pose of the capture point frame relative to the end-effector frame can be determined from the measurement of the base stereo vision and the current angles. Then the trajectories of the joints for capturing can be planned using the autonomous path planning proposed by the authors in the previous works.[25]

5.3. The coordinated plan and control of the base and the manipulator

Sections 5.1 and 5.2 respectively introduce the GNC of the chaser and the path planning of the space manipulator. If the manipulator is not operated or the disturbance resulting from the manipulator's motion is very small, the separated GNC (independent on the manipulator's controller) is adequate for the control of the base. On the other hand, when the base is not controlled (free floating) or the manipulator is under the 'Spacecraft-Referenced End-Point Motion Control',[26] the separated path planning approach (independent on the GNC of the base) can also be used. However, in order to improve the control performance of the whole system during the capturing, the GNC of the base and the control of the manipulator are required to work in a coordinated mode. So we propose the coordinated plan and control (CP&C) method, which is actually a coordinated management of the methods of Sections 5.1 and 5.2. The basic concept is shown as Fig. 14.

First, the position and orientation of the target is measured, and its trajectory is predicted. Then the 'Desired Rendezvous Pose' of the base is determined according to the measured and predicted results. And, the trajectories of the base pose and the joint angle are planned in 'coordinated behaviour'. The so-called 'coordinated behaviour' is that the motion of the joints and the base is planned cooperatively, considering the other one's motion in its own planning iteratively. The estimated position and attitude of the base at next sampling time will be included in the planning of the joint trajectory of the manipulator, and the possible disturbance resulting from the planned motion of the manipulator is considered in the planning of the base. Lastly, the coordinated controllers of the base and the joints are designed to drive the base and the joints to follow the desired motions. Using the method, a target moving with somewhat arbitrary trajectory can be captured by the space robotic system with the 'Desired Rendezvous Attitude'.

https://doi.org/10.1017/S0263574709990397 Published online by Cambridge University Press

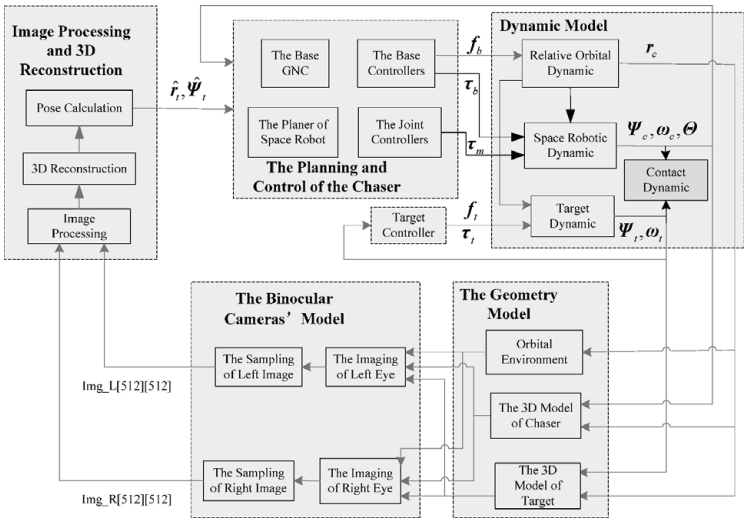

Fig. 15. The structure of 3D simulation system for the automatic rendezvous and robotic capturing.

6. Simulation Study

6.1. The 3D simulation system

In order to verify the proposed approach, a 3D simulation system is developed in VC environment. The system is composed of six modules (see Fig. 15): *Image Processing and 3D Reconstruction*, *the Planning and Control of the Chaser*, *the Target Controller, the Dynamic Model*, *the Geometry Model* and *the Binocular Cameras Model*. The *Image Processing and 3D Reconstruction* processes the images of the binocular stereo cameras (image filtering, edge detection and line extraction), and supplies the relative pose of the target (recognizing the solar panel support, obtaining the 3D coordinates of the features and calculation of the target pose). *The planning and control of the chaser* plans the motions of the space robotic system (the position, attitude of the base and the joint trajectories of the manipulator), and drives the space robotic system to track the planned motions. The *Target Controller* generates the control forces and torques to drive the target move in some given rules, emulating the target with a certain moving state, such as three axis stabilization, spin stabilization or tumbling. The *Dynamic Model*, including the relative orbital dynamic model, space robotic dynamic model target dynamic model, and the contact dynamic.[14] The inputs of the *Dynamic Model* are the driving forces or toques of each DOF (degree of freedom), and the outputs are the position and velocity of each DOF. The *Geometry Model* draws and displays the 3D graphics of the chaser and target in real-time, according to the states output from the 'Dynamic Model'. The 3D models, including the orbital environment, the models of the chaser and the target, are created using OpenGL. An example is shown in Fig. 6. *The Binocular Cameras Model* supplies the emulated images of the cameras, which is detailed in 4.2.1.

6.2. Simulation study of autonomous rendezvous and robotic capturing

6.2.1. The initial conditions. The initial poses of the chaser and target are the same as Eqs. (12)–(15). The 3D model corresponding to the initial state of the system is shown in Fig. 6.

The initial linear velocity of the chaser's CM (system's CM) relative to the target orbital frame is

$$^{O_2}\boldsymbol{v}_{O1} = [10\,\text{mm/s},\ 10\,\text{mm/s},\ 10\,\text{mm/s}]\,. \tag{45}$$

And the angular velocity of the chaser's base is

$$^{O_2}\boldsymbol{\omega}_b = [0.5^o/s, 0.5^o/s, 0.5^o/s]. \tag{46}$$

The target is assumed to three-stabilized, i.e. it is controlled to attain the desired attitude $\boldsymbol{\Psi}_{td}$ with the initial angular velocity $^{O_2}\boldsymbol{\omega}_{t0}$ given as follows:

$$\boldsymbol{\Psi}_{td} = [6^o, -5^o, 7^o], \tag{47}$$

$$^{To}\boldsymbol{\omega}_{t0} = [0.5^o/s, 0.5^o/s, 0.5^o/s]. \tag{48}$$

6.2.2. The simulation results. The proposed method is used for the chaser to rendezvous with and capture the non-cooperative target. The desired rendezvous pose of the chaser with respect to the target is designed as

$$\begin{cases} ^{R1}\boldsymbol{r}_{R2}^{R1} = [1.6000 \quad 0.0000 \quad 0.0000]^T \\ ^{R1}\boldsymbol{\Psi}_{R2} = [0.0000 \quad 0.0000 \quad 0.0000]^T \end{cases}. \tag{49}$$

The simulation results are shown as Figs. 16–22. The relative position and attitude tracking trajectory and the tracking errors are shown in Figs. 16 and 17 respectively. When the chaser approaches the target within the given thresholds of $^{R1}\boldsymbol{r}_{R2}^{R1}$ and $^{R1}\boldsymbol{\Psi}_{R2}$ (in this paper, the position threshold is 0.05 m and the attitude threshold is 3°), the manipulator is commanded (at $t = 68.25$ s) to capture the target. The motions of the manipulator joints are shown in Fig. 18, and the end-effector's pose with respect to the capture point varies as Fig. 19. The approaching zeros (at $t = 116.5$ s) implie that if the target is in the reach of the end-effector, the end-effector can capture the target. Figures 20–22 give some typical states. The chaser reaches at the desired pose given

https://doi.org/10.1017/S0263574709990397 Published online by Cambridge University Press

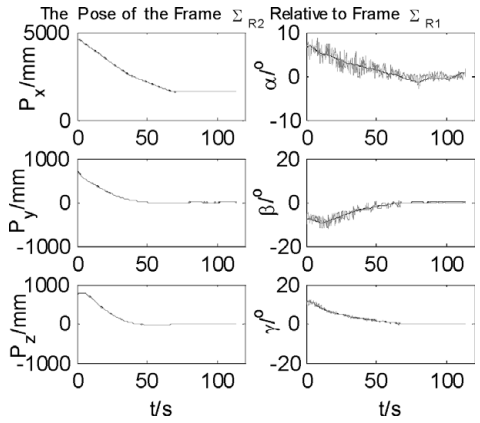

Fig. 16. The pose tracking during the rendezvous and capturing (0 s $\leq t \leq$ 116.5 s).

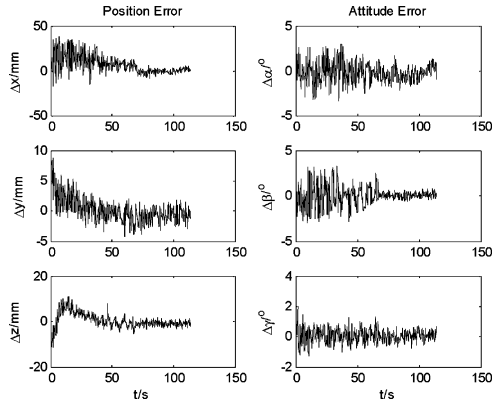

Fig. 17. The pose tracking errors during the rendezvous and capturing (0 s $\leq t \leq$ 116.5 s).

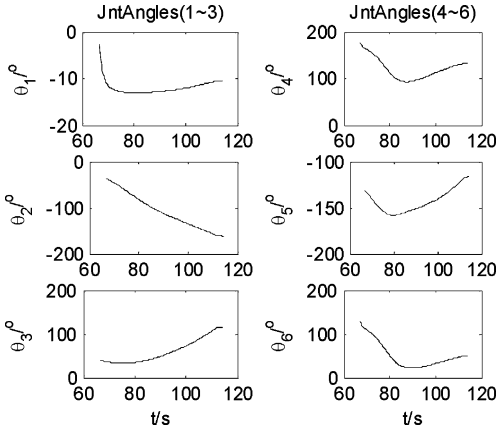

Fig. 18. The variation of the joint angles during capturing (68.25 s $\leq t \leq$ 116. 5 s).

by Eq. (49) at $t = 68.25$ (see Fig. 21); then the manipulator is commanded to capturing the target panel support. At $t =$ 116.5 s, the target is grasped by the end-effector and the mission is finished, shown as Fig. 22.

The simulation results show that the proposed approach for measure the pose of the target is feasible for the GNC of the chaser, and the path planning and control of the space manipulator during the autonomous rendezvous and capturing. The trajectory tracking errors are less than 0.045 m and the attitude tracking errors are less than 3°. The nearer the distance is, the less the errors are. When the distance

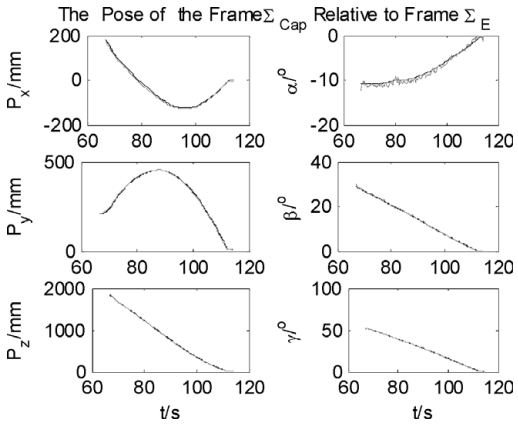

Fig. 19. The pose tracking of the end-effector during the capturing (68.25 s $\leq t \leq$ 116.5 s).

is smaller than 2 m, the errors are less than 0.02 m and 1.5° respectively. The main errors sources are as follows: (1) the noise existing in the original images; (2) the errors resulting from the image processing. It is impossible for the Canny edge detection and Hough Transform algorithms themselves to detect and extract the ideal edges and lines, since a certain parameters used by the algorithms determine the processing speed and accuracy. The general handling is to obtain a trade-off between the speed and accuracy; (3) time delay resulting in larger tracking errors. There exists non-negligible time delay from the time of image acquisition to that of the measurement results coming out. The target is moving with respect to the chaser. So the time delay results measurement errors. It is analyzed that the time delay is approximately 0.5 s, which generates about 0.02 m and 1.5° differences (the approach linear velocity and angular velocity of the chaser are about 0.04 m/s and 3°/s respectively).

7. Discussion and Conclusion

In this paper, we proposed a method for autonomous rendezvous with and capturing a non-cooperative object in space. Part contents of this paper (such as Section 4.2.6) actually aim at the case of a triangle panel support, since a concrete mechanism is required to be taken as the recognized and captured object. Considering the technology level of today, it is very difficult to use only such simple sensors (including their software) to recognize a target of arbitrary shape. A possible method is to design multi-sensors (mounted on the chaser), whose information is fused to supply measurement results, to enlarge the versatility. But it will largely increase the cost (money, mass and power) of devices and complexity of the algorithms, which affect the real time applications. Therefore, the most rational handling is to develop a library of algorithms which can measure the pose of targets with typical shapes. When the space robot is designated to service a certain satellite, the corresponding algorithm in the library can be directly used. Developing such a library is our purpose in the near future. In this paper, we handled the problem of a satellite with triangle panel supports.

Moreover, the collision is a danger during the grasping. In the proposed method, the manipulator autonomously

https://doi.org/10.1017/S0263574709990397 Published online by Cambridge University Press

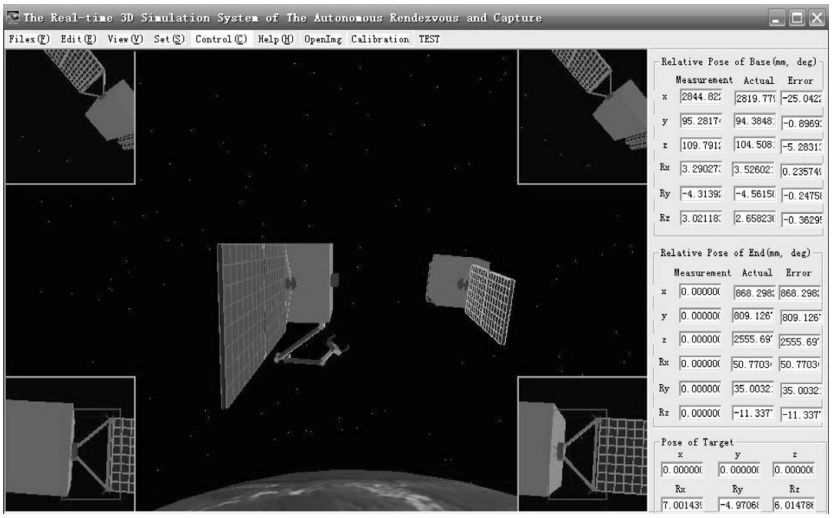

Fig. 20. The temporary state for the simulation at $t = 43.25$ s.

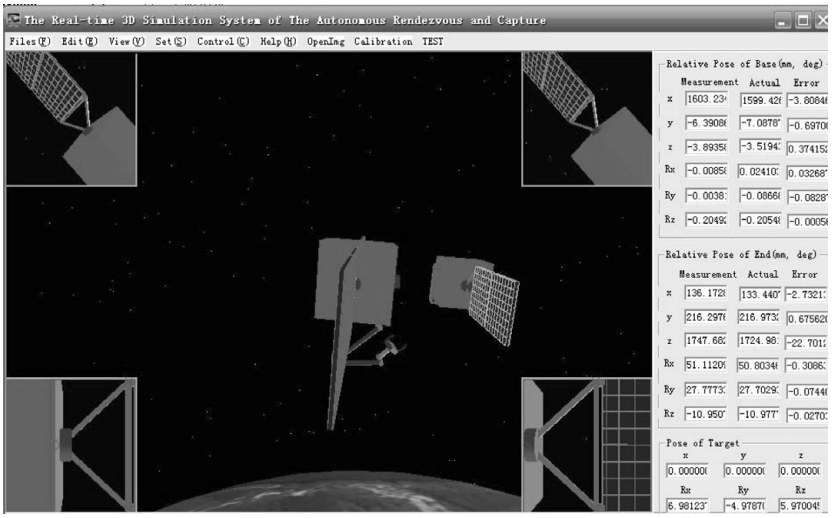

Fig. 21. The chaser reaches at the desired pose and the manipulator is commanded at $t = 68.25$ s.

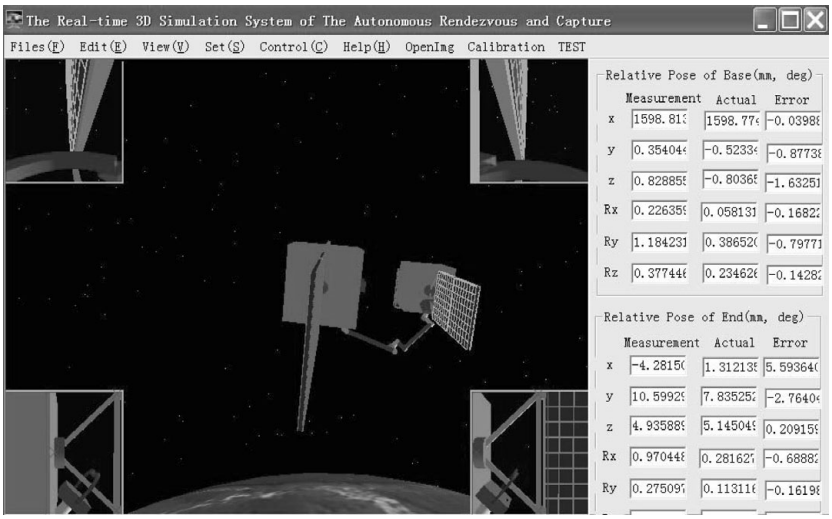

Fig. 22. The final state for the simulation ($t = 116.5$ s).

https://doi.org/10.1017/S0263574709990397 Published online by Cambridge University Press

adjusts its motion according to the pose measurement and the predictive results on real time. If the output frequencies of the sensor (now 4 Hz for the visual measurement) and the controllers (200 Hz for the joint controller) are high enough, or the target is relative stable, the collision possibility is low. But advanced algorithms are also required to avoid unfavourable collision, especially for a tumbling target. This is also a problem to be solved in the future.

Acknowledgements

This work is supported by National Nature Science Foundation of China (No. 60805033), and China Postdoctoral Science Foundation under research grants (No. 20080440116).

References

1. G. Hirzinger, K. Landzettel, B. Brunner, M. Fischer and C. Preusche, "DLR's robotics technologies for on-orbit servicing," *Adv. Robot.* **18**(2), 139–174 (2004).
2. K. Landzettel, C. Preusche, A. Albu-Schaffer and D. Reintsema, "Robotic On-Orbit Servicing – DLR's Experience and Perspective," *Proceedings of IEEE/RSJ International Conference on Intelligent Robots and Systems*, Beijing, China (2006) pp. 4587–4594.
3. K. Yoshida, "Engineering test satellite VII flight experiments for space robot dynamics and control: Theories on laboratory test beds ten years ago, now in orbit," *Int. J. Robot. Res.* **22**(5), 321–335 (2003).
4. J. R. Wilson, "Satellite hopes ride on orbital express," *Aerosp. Am.* **45**(2), 30–35(2007).
5. B. Liang, C. Li, L. J. Xue and W. Y. Qiang, "A Chinese Small Intelligent Space Robotic System for On-Orbit Servicing," *Proceedings of IEEE/RSJ International Conference on Intelligent Robots and Systems*, Beijing, China (2006) pp. 4603–4607.
6. M. Oda, "Motion control of the satellite mounted robot arm which assures satellite attitude stability," *Acta Astron.* **41**(11), 739–750 (1997).
7. M. Oda, "Space Robot Experiment on NASDA's ETS-VII satellite," *Proceedings of IEEE International Conference on Robotics and Automation*, Detroit, MI (1999), pp. 1390–1395.
8. J. Shoemaker and M. Wright, "Orbital Express Space Operations Architecture Program," *Proceedings of SPIE – The International Society for Opt. Eng.*, Orlando, FL, United States (2003) pp. 1–9.
9. G. Hirzinger, B. Brunner and K. Landzettel, "Space robotics-dlr's telerobotic concepts, lightweight arms and articulated hands," *Autonom. Robot.* **14**, 127–145 (2003).
10. B. Bischof and Astrium GmbH, "Roger – Robotic Geostationary Orbit Restorer," *Proceedings of 54th International Astronautical Congress of the International Astronautical Federation*, Bremen, Germany (2003) IAC-03-IAA.5.2.08.
11. J. K. Thienel, J. M. VanEepoel and R. M. Sanner, "Accurate State Estimation and Tracking of a Non-Cooperative Target Vehicle," *Proceedings of AIAA Guidance, Navigation, and Control Conference*, Keystone, CO, (2006) pp. 5511–5522.
12. K. Yoshida, H. Nakanishi, H. Ueno, N. Inaba, T. Nishimaki and M. Oda, "Dynamics, control and impedance matching for robotic capture of a non-cooperative satellite," *Adv. Robot.* **18**(2), 175–198 (2004).
13. H. Nakanishi and K. Yoshida, "Impedance Control for Free-Flying Space Robots – Basic Equations and Applications," *Proceedings of The IEEE/RSJ International Conference on Intelligent Robots and System*, Beijing, China (2006) pp. 3137–3142.
14. D. N. Nenchev and K. Yoshida, "Impact analysis and post-impact motion control issues of a free-floating space robot subject to a force impulse," *IEEE Trans. Robot. Autom.*, **15**(3), 548–557 (1999).
15. W. Fehse, *Automated Rendezvous and Docking of Spacecraft* (Cambridge University Press, Cambridge, MA, 2003).
16. Y. S. Xu and T. Kanade, *Space Robotics: Dynamics and Control* (Kluwer Academic Publishers, Norwell, Massachusetts, 1992).
17. S. A. Moosavian and E. Papadopoulos, "Free-flying robots in space: An overview of dynamics modeling, planning and control," *Robotica* **25**(5), 537–547 (2007).
18. T. Weismuller and M. Leinz, "GN&C Technology Demonstrated by the Orbital Express Autonomous Rendezvous and Capture Sensor System," *Proceedings of the 29th Annual AAS Guidance and Control Conference*, Breckenridge, CO (2006) AAS 06–016.
19. W. Chang, "Binocular vision-based 3-D trajectory following for autonomous robotic manipulation," *Robotica* **25**, 615–626 (2007).
20. R. Anchini, C. Liguori, V. Paciello and A. Paolillo, "A comparison between stereo-vision techniques for the reconstruction of 3-D coordinates of objects," *IEEE Trans. Instrum. Meas.* **55**(5), 1459–1466 (2006).
21. L. M. Song, M. P. Wang, L. Lu and H. J. Huan, "High precision camera calibration in vision measurement," *Optics & Laser Technol.* **39**, 1413–1420 (2007).
22. W. Kim, R. Steinke, R. Steele and A. Ansar, "Camera calibration and stereo vision technology validation report," *JPL D-27015*, 1–82 (2004).
23. O. A. R. Board, D. Shreiner, M. Woo, J. Neider and T. Davis, *OpenGL(R) Programming Guide: The Official Guide to Learning OpenGL(R)* (Addison-Wesley Professional, 2005).
24. M. Sonka, V. Hlavac and R. Boyle, *Image Processing, Analysis, and Machine Vision*, 3rd ed. (Cengage-Engineering, 2007).
25. W. F. Xu, B. Liang, C. Li, Y. Liu and Y. S. Xu, "Autonomous target capturing of free-floating space robot: Theory and experiments," *Robotica* **27**, 425–445 (2009).
26. E. Papadopoulos and S. Dubowsky, "On the nature of control algorithms for free-floating space manipulators," *IEEE Trans. Robot. Autom.* **7**(6), 750–758 (1991).